Acta Oceanol. Sin., 2019, Vol. 38, No. 3, P. 36–44
https://doi.org/10.1007/s13131-019-1397-3
http://www.hyxb.org.cn
E-mail: hyxbe@263.net

The vertical heat transport of internal solitary waves over the continental slope in the northern South China Sea

Changrong Liang[1, 2], Xiaodong Shang[1]*, Guiying Chen[1]

[1] State Key Laboratory of Tropical Oceanography, South China Sea Institute of Oceanology, Chinese Academy of Sciences, Guangzhou 510301, China

[2] University of Chinese Academy of Sciences, Beijing 100049, China

Received 20 October 2017; accepted 11 November 2017

Abstract

An integrated analysis of internal solitary wave (ISW) observations obtained from two moorings over the continental slope in the northern South China Sea (SCS) leads to an assessment of the vertical heat transport of the ISWs. The clusters of ISW packets are phase-locked to the fortnightly cycle of the semidiurnal tide. The ISWs appear during large semidiurnal tides, and there is a period of 5–6 d when no ISWs are observed. The effect of the ISWs on the continental slope heat budget is observed. The ISWs can modify a local temperature field in which the temperature in the upper layer can be changed by O (10^0) °C after the ISWs passed the mooring. Both ISW-induced diffusion and ISW-induced advection contribute to the temperature variation. The estimates imply an average vertical heat flux of 0.01 to 0.1 MW/m^2 in the ISWs in the upper 500 m of the water column. The vertical heat transport ranges from 0.56 to 2.83 GJ/m^2 with a mean value of 1.63 GJ/m^2. The observations suggest that the vertical heat transport is proportional to the maximum vertical displacement.

Key words: internal solitary wave, vertical heat transport, temperature variation, diffusion, advection, vertical heat flux

Citation: Liang Changrong, Shang Xiaodong, Chen Guiying. 2019. The vertical heat transport of internal solitary waves over the continental slope in the northern South China Sea. Acta Oceanologica Sinica, 38(3): 36–44, doi: 10.1007/s13131-019-1397-3

1 Introduction

Nonlinear internal solitary waves (ISWs) are a ubiquitous feature in the ocean. They carry large amounts of energy and momentum as they propagate (Klymak et al., 2006; Lien et al., 2005). The ISWs can reach the breaking limit as they shoal, producing enhanced turbulent mixing (Lien et al., 2014, 2012). Strong momentum and enhanced turbulent mixing induced by the ISWs suggest that the ISWs are a fundamental contributor to the redistribution of nutrients and heat. Elevated heat fluxes in the ISWs have been reported over the continental shelf (Moum et al., 2003; Inall et al., 2000; Shroyer et al., 2010). Inall et al. (2000) estimated the average heat flux across the thermocline to be 80 W/m^2 over the Malin shelf during the large-amplitude high-frequency ISWs; Moum et al. (2003) reported an instantaneous heat flux in the ISWs of O (10^3) W/m^2 over the continental shelf of Oregon; Shroyer et al. (2010) estimated the instantaneous heat flux in the ISWs to be 790 W/m^2 over New Jersey's shelf, which was one order of magnitude greater than the background value. These observations indicated that the enhancement of heat flux in the ISWs over the continental shelf is primarily attributed to the ISW-induced diffusion.

The South China Sea (SCS), which is one of the largest marginal seas of the Pacific, is well known as a location where the ISWs have been commonly observed. The ISWs originate in the Luzon Strait and propagate westward across the deep basin until they encounter the continental shelf (Guo and Chen, 2014; Ramp et al., 2004), which can be observed in Synthetic Aperture Radar (SAR) imagery (Hsu et al., 2000; Liu and Hsu, 2004). In addition to these ISWs originating in the Luzon Strait, the ISWs can also be generated locally at the shelf break by the evolution of the internal tides due to nonlinear and dispersive effects (Xu et al., 2010). Although there have been numerous studies of the ISWs in the northern SCS (Orr and Mignerey, 2003; Ramp et al., 2010; Alford et al., 2010, 2011; Bai et al., 2014; Chen et al., 2014), most studies have focused on the generation, characteristics, propagation patterns and energy contents of the ISWs, but few studies have focused on the vertical heat transport of the ISWs. Here we report the vertical heat transport of the ISWs over the continental slope in the northern SCS using data collected in autumn 2014. Our observations indicate that both ISW-induced advection and ISW-induced diffusion contribute to the redistribution of heat, and the magnitude of depth-integrated heat has a positive relationship with the maximum vertical displacement. We continue in Section 2 with a description of our experimental area and moored instrumentation. The results are presented in Section 3, which is divided into two parts. First, the arrivals of the ISWs are documented and their implied relationship with the internal tides is discussed. Second, we estimate the vertical heat transport of the ISWs and discuss the relationship between the vertical heat transport and the vertical displacement. A discussion and con-

Foundation item: The National Natural Science Foundation of China under contract Nos 41676022, 41630970 and 41521005; the National Programme on Global Change and Air-Sea Interaction under contract No. GASI-IPOVAI-04; the Open Project Program of State Key Laboratory of Tropical Oceanography under contract No. LTOZZ1801; the Instrument Developing Project of the Chinese Academy of Sciences under contract No. YZ201432.
*Corresponding author, E-mail: xdshang@scsio.ac.cn

clusions are provided in Sections 4 and 5, respectively.

2 Measurements

On 1 August 2014 two moorings (A and B) were deployed over the continental slope in the northern SCS (Figs 1a and b). The deployment lasted for 59 d, from 1 August to 27 September 2014, providing a description of the surface and internal tides and, in particular, the velocity and temperature structures of the ISWs. Mooring B (20.84°N, 117.56°E) was located 22.13 km away from Mooring A (20.74°N, 117.75°E). The water depths of Moorings A and B were approximately 1 260 and 850 m, respectively. Mooring A was equipped with one upward-looking 75 kHz ADCP at 440 m depth, one downward-looking 75 kHz ADCP at 450 m depth, one downward-looking 150 kHz ADCP at 950 m depth, two Sea-Bird Electronics CTD sensors, 15 temperature sensors, and 14 conductivity/temperature (CT) sensors. The upward-looking and downward-looking 75 kHz ADCPs pinged and recorded data at 2 min interval with a vertical resolution of 16 m. The downward-looking 150 kHz ADCP pinged and recorded data at 1.5 min interval with a vertical resolution of 8 m. All of the CTD and temperature sensors sampled at 10 s interval, and the CT sensors sampled at 15 s interval. Mooring B was equipped with one upward-looking 75 kHz ADCP at 500 m depth, one downward-looking 75 kHz ADCP at 520 m depth, two Sea-Bird Electronics CTD sensors, 12 temperature sensors, and nine CT sensors. Both 75 kHz ADCPs pinged and recorded at data 2 min interval with a vertical resolution of 16 m. All of the CTD and temperature sensors sampled at 10 s interval, and the CT sensors sampled at 15 s interval. The ADCP relies on sufficient natural scatters in the water column to create a good return signal, but the ADCP cannot capture sufficient natural scatters every time. Data that comprised less than 80% good natural scatters were rejected, and the occasional unrealistic extreme values (e.g., speeds of being greater than 10 m/s) were removed. If the absent data points had good adjacent values in either time or space, then they were estimated using linear interpolation. Data from Mooring A were used to explore the characteristics of the ISWs and estimate the vertical heat transport of the ISWs, whereas data from Mooring B were combined to calculate the phase speed of the ISWs.

3 Results

3.1 *Arrival of internal solitary waves*

We analyzed the scale and arrival of the ISWs using the data obtained from Mooring A. To clearly show the scale and arrival of the ISWs, we applied high-pass filtering of 1.0 h^{-1} to the temperature signal at 250 m. The high-pass filtered temperature fluctuations (Fig. 1c) clearly provide an overall impression of the scale and arrival of the ISWs. All of the observed ISWs were depression waves, such that a pronounced increase in temperature was observed as the ISWs passed the mooring. The largest temperature fluctuation induced by the ISWs was 8.5°C. Five clusters of the ISW packets were observed during the measurements, where the

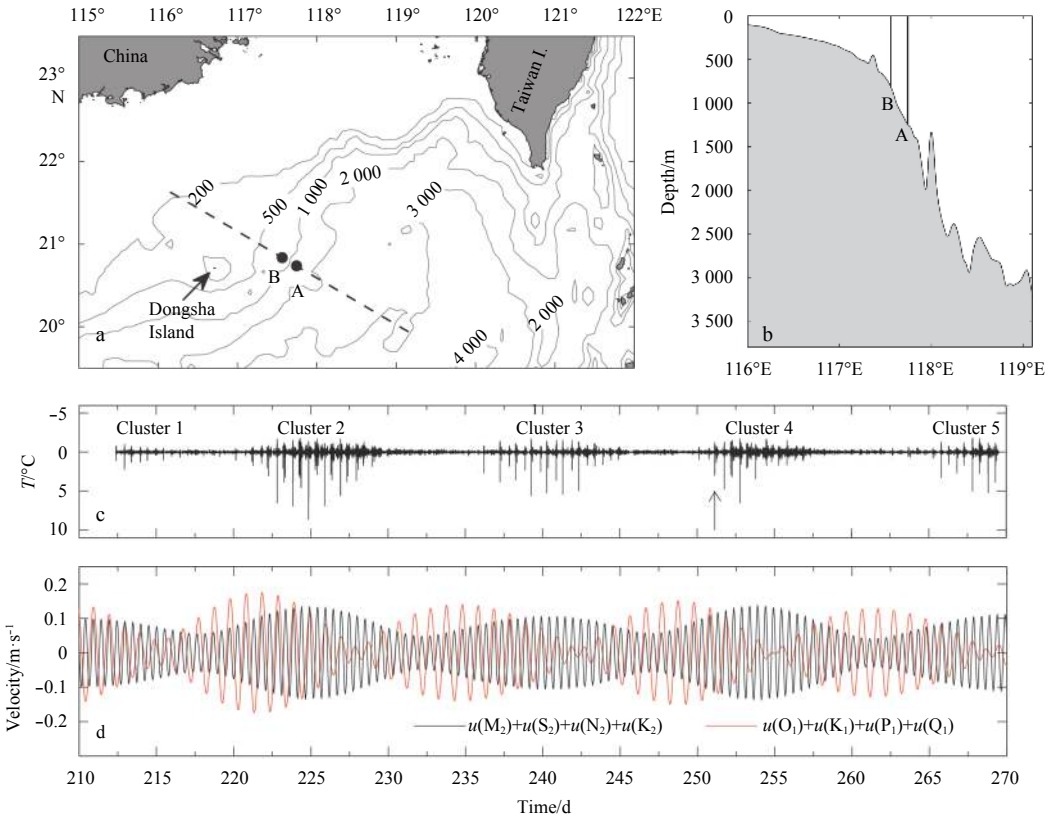

Fig. 1. Observation sites and arrival of internal solitary waves. a. Bottom topography of the northern South China Sea and mooring distribution of the experiment. The black dots indicate the locations of moorings. b. Bathymetry profile along the dashed line shown in Figs 1a and c. Time series of the high-pass filtered (1.0 h^{-1}) temperature fluctuations at 250 m. The arrow indicates the example of the ISW shown in Fig. 3d. Time-series of the barotropic tidal velocity in the Luzon Strait predicted from the global inverse tide model (TPXO).

amplitudes of Cluster 2 waves were much greater than those of other cluster waves. The ISWs typically form from internal tides that are generated by tidal flow over topography in the Luzon Strait (Li and Farmer, 2011). To explore the relationship between the ISWs and the barotropic tides in the Luzon Strait, we obtained the barotropic tides in the Luzon Strait (20.5°N, 121.0°E) using the global inverse tide model (TPXO) (Egbert and Erofeeva, 2002), which provides the timing of diurnal and semidiurnal tides in the Luzon Strait during the period of observation. The distance between Mooring A and the Luzon Strait (20.5°N, 121.0°E) is approximately 341 km. With the mean phase speed of ISWs of 3.11 m/s (Table 1), we can estimate the time that is necessary for the ISWs to propagate from the Luzon Strait to Mooring A. The estimated propagation time is approximately 1.27 d. Figure 1d shows the resultant tides of tidal frequencies. The propagation time of the ISWs was offset. The fortnightly cycles were well-represented in both the resultant diurnal tide $[u(O_1)+u(K_1)+u(P_1)+u(Q_1)]$ and the resultant semidiurnal tide $[u(M_2)+u(S_2)+u(N_2)+u(K_2)]$. A comparison of the high-pass filtered temperature fluctuations (Fig. 1c) to the resultant tides (Fig. 1d) clearly provides an overall impression of the arrival of the ISWs. The clusters of the ISW packets were clearly phase-locked to the fortnightly cycle of the semidiurnal tide. The ISWs appeared during large semidiurnal tides and there is a period of 5–6 d (during small semidiurnal tides) when no ISWs were observed.

Table 1. Summary of phase speed (c), wave amplitude (a), half width (λ), maximum vertical displacement (δ_{max}), and heat transport (E_Q)

	c/m·s^{-1}	a/m	λ/m	δ_{max}/m	E_Q/J·m^{-2}
Range	2.55–3.82	45–195	795–2 568	13.2–158.5	(0.56–2.82)×10^9
Mean	3.11	86	1 382	70.8	1.63×10^9
Std.	0.26	34.4	415.2	35.8	0.58×10^9

Note: Std. represents standard deviation.

To further explore the features of the ISWs, we plot samples of time series of the vertical velocity in Fig. 2. These time series span from 236 to 242 d (Fig. 1d, during large semidiurnal tides). There are no ISWs in 235 d (not shown), and only one ISW occurs in 236 d. As the semidiurnal tide became strong (Figs 1c and d), more ISWs occurred per day. As is shown in Fig. 2, three ISWs occurred each day in the following 4 d (237–240 d). The number of the ISWs decreases again as the semidiurnal tide became weak (241 and 242 d). For simplicity, we define the three ISWs that occurred in 1 d as S1, S2 and S3, respectively. S1 appeared in the morning (05:00–09:00 o'clock) and S2 appeared approximately 2 h after the appearance of S1. S2 had small amplitudes but were independent of S1. S3 appeared during the nighttime (20:00–22:00 o'clock). S3 was weaker than S1 but stronger than S2. S1 arrived approximately 30 min later each day, and S2 arrived approximately 15 min later each day. These time lags were smaller than those over the continental shelf that were reported by Ramp et al. (2004). More observations are needed to explain this difference.

3.2 *Vertical heat transport of internal solitary waves*

One of the ISWs from Mooring A is shown in Fig. 3, which provides more details about the current and temperature structures of the ISWs. This ISW arrived at Mooring A on 251.15 d (Fig. 1c, indicated by the arrow). Only zonal velocity is shown because the ISWs propagated principally westward and most of the velocities were contained in the zonal velocity. The ISW had opposing zonal currents in the upper (<225 m) and lower (>225 m) layers, with the maximum westward current in the upper layer reaching 1.4 m/s (Fig. 3a). The nodal point where the zonal velocity was 0 was at 225 m, which is deeper than those observed over the continental shelf (Lien et al., 2014). The vertical velocity (Fig. 3b) shows a

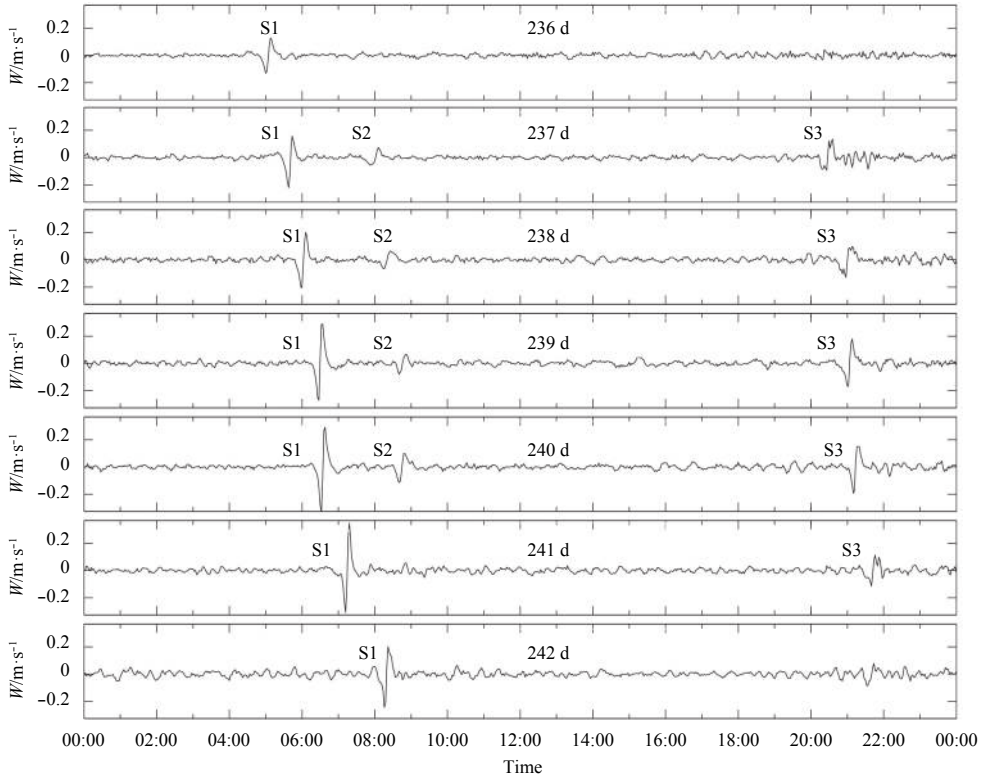

Fig. 2. Time-series of the vertical velocity from 236 to 242 d. S1, S2 and S3 represent the ISWs.

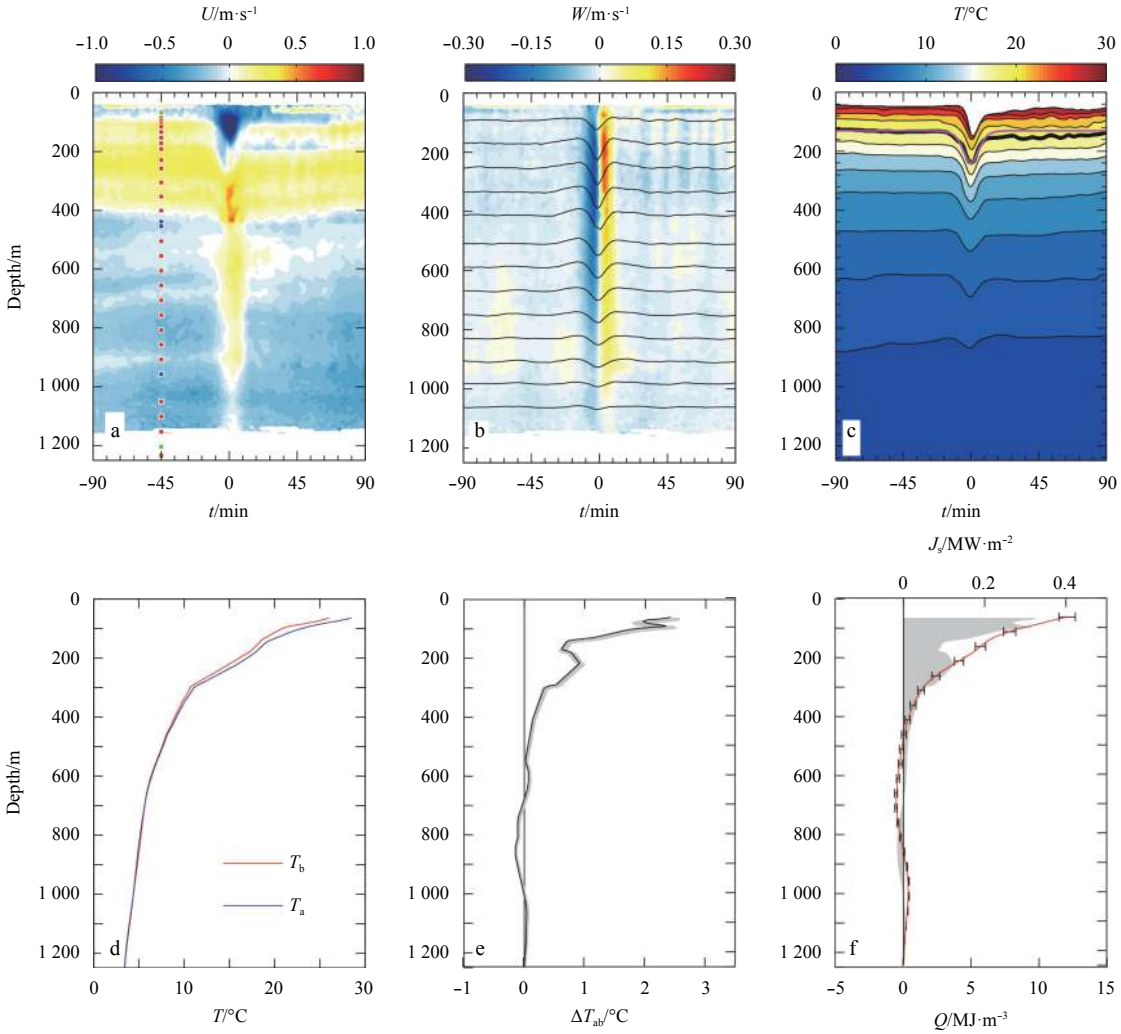

Fig. 3. Velocity, temperature, and heat transport during the ISW. a–c. Contour plots of zonal velocity, vertical velocity, and temperature of the ISW observed on 251.15 d. The dots in Fig. 3a indicate the averaged depths of temperature and CT sensors (red), CTDs (green), and ADCPs (blue). The black curves overlain on Fig. 3b are the vertical displacements (δ). The thick black curve in Fig. 3c highlights the isotherm that experienced the maximum vertical displacement and the pink curve shows the sech^2 permanent form wave solutions of the KdV equation. d. The profiles of T_b and T_a. e. The profile of ΔT_{ab}. The gray shading indicates the 95% bootstrapped confidence interval for ΔT_{ab}. f. The profiles of the net heat transport Q (gray shading) and the heat flux J_s in the ISW (red curve). The 95% bootstrapped confidence interval is plotted for J_s.

classic first-mode depression wave structure with a sharp downward vertical velocity followed by an upward vertical velocity. We estimated the vertical displacement (δ) using vertical velocity data (Inall et al., 2001), which is defined as

$$\delta(z,t) = \int_{t_0}^{t} W_f(z,t)\,\mathrm{d}t,$$

where t_0=–90 min and $W_f(z, t)$ is the high-pass filtered (1 h^{-1}) vertical velocity signal at depth z. The results are shown in Fig. 3b. Large vertical displacements were observed between the two vertical pulses with the maximum vertical displacement (δ_{max}) reaching 72 m. In total, 75 ISWs were encountered during the observation period. A summary of the maximum vertical displacement in the observed ISWs is given in Table 1. The maximum vertical displacement shows large variation; and these values range from 13.2 to 158.5 m, with a mean value of 70.8 m and a standard deviation of 35.8 m.

Figure 3c shows the isotherms of the ISW. The temperature sensors in the upper layer were pressed down to the deep water during the passage of the ISW as the mooring was bent over by drag forces, thus there are no temperature data in the upper layer during the passage of the ISW (the white patch in Fig. 3c). The depths of the temperature/CT sensors during the passage of the ISW were calculated based on the depths of the CTDs and the ADCPs. There are two cases for the sinking of the temperature/CT sensors. In the first case, we assume that the sinking of the temperature/CT sensors resulted from the tilting of the mooring. The depths that were calculated from this case were the lower limits of the temperature/CT sensors. In the second case, we assume that the sinking of the temperature/CT sensors resulted from the vertical sinking of the mooring. The depths calculated from this case were the upper limits of the temperature/CT sensors. The first case is more likely to be accurate. As indicated in Figs 3a and b, the horizontal velocity was much stronger than the vertical velocity in the upper 200 m. Thus upper instruments

were advected horizontally by the horizontal velocity, which resulted in the tilt of mooring, rather than vertical depressed by the vertical velocity, and caused the mooring to sink vertically. Here we calculated the depths of the temperature/CT sensors during the passage of the ISW by assuming that the sinking of the temperature/CT sensors resulted from the tilting of the mooring, which provides the lower limits of the temperature/CT sensors.

Isotherms were first depressed downward by the downward vertical velocity and were then lifted up by the upward vertical velocity. The maximum isotherm displacement reached 109 m (Fig. 3c, indicated by the thick black curve). Figure 3c also shows the steady wave-like solutions of the Korteweg-deVries (KdV) equation (Moum et al., 2003; Choi and Camassa, 1999), $\zeta(x,t) = a\,\mathrm{sech}^2\left[(x-ct)/\lambda\right]$, where a=109 m, is the wave amplitude; c=3.0 m/s, is the phase speed; and λ=1 277 m, is the half width of the wave. Moorings A and B are nearly located along the direction of propagation of the ISWs (Liu et al., 2004; Xu et al., 2016) and the distance between them was small. Therefore, the phase speed was roughly estimated by dividing the horizontal separation (22.13 km) between Moorings A and B by the corresponding elapsed time (1.98 h), and then subtracting the mean tidal speeds of $O(0.1)$ m/s. The ISW traveled faster than those observed by Lien et al. (2014) in shallow water (<500 m), whose measured phase speeds of the ISWs were smaller than 2.5 m/s. The large phase speeds observed here are consistent with the theory (Small, 2001a, b) that the phase speeds decrease as the ISWs shoal. The shape of the ISW is quite close to sech^2 form (Fig. 3c, indicated by the pink curve), indicating that the ISWs can be described by the weakly nonlinear KdV equation. Different ISWs had different phase speeds, wave amplitudes, and half-widths. A summary of the phase speeds, the wave amplitudes, and the half-widths is given in Table 1. The phase speeds range from 2.55 to 3.82 m/s, with an average of 3.11 m/s. The small value (0.26 m/s) of standard deviation indicates that the phase speeds of the ISWs were relatively stable. The wave amplitude, instead, was more variable. These values range from 45 to 195 m with a mean value of 86 m and a standard deviation of 34.4 m. Evidence of variable wave amplitudes can also be observed in the time-series of high-pass filtered temperature fluctuations in Fig. 1c. The half width also shows variation, ranging from 795 to 2 568 m with a mean value of 1 382 m and a standard deviation of 415.2 m.

A prominent feature in Fig. 3c is that the observed isotherms after the passage of the ISW (t>25 min) were deeper than those before the ISW (t<–25 min), which implies an increase in the temperature after the ISW passed the mooring. The profiles of $T_b(z)$ and $T_a(z)$ are shown in Fig. 3d and their difference, $\Delta T_{ab}(z)=T_a(z)-T_b(z)$, is shown in Fig. 3e. $T_b(z)$ was the average temperature at depth z between –90 and –25 min on the time axis in Fig. 3c, corresponding to the period when the temperature field was not influenced by the ISW and $T_a(z)$ was the average temperature at depth z between 25 and 90 min, corresponding to the period when the ISW had passed the mooring. $\Delta T_{ab}(z)$ represented the temperature variation at depth of z induced by the ISW. ΔT_{ab} showed a decreasing trend with depth and became insignificant at approximately 500 m. The maximum of ΔT_{ab} occurred in the topmost layer with a value of 2.45°C. A small peak value of ΔT_{ab} was observed at 215 m.

An increase in the temperature after the passage of the ISW indicates that the heat is redistributed by the ISW. To quantify how much heat was transported into the lower layer by the ISW, we estimated the net heat transport of the ISW using:

$$Q(z) = \rho_a(z)\, c_p T_a(z) - \rho_b(z)\, c_p T_b(z)\,, \tag{1}$$

where ρ_b and ρ_a are the water densities; and c_p=3.986 kJ/(kg·°C) is the specific heat that describes the amount of heat needed to raise the temperature of a certain mass by 1°C. The estimated Q induced by the ISW is shown in Fig. 3f. The downward-decreasing trend of Q is similar to that of ΔT_{ab}. A small peak value of Q was also observed at 215 m, corresponding to the peak value of ΔT_{ab} at 215 m (Fig. 3e). The heat transport was mainly limited in the upper ocean with 98% of Q occurring in the upper 500 m.

The heat flux during the passage of the ISW was estimated by integrating Q in the water column, $J_s(z) = \dfrac{1}{\Delta t}\displaystyle\int_{z_b}^{z} Q(z)\,\mathrm{d}z$, where Δt=50 min, represents the time that the ISW needed to pass the mooring and z_b represents the ocean bottom. The profile of J_s is shown in Fig. 3f. J_s shows a downward-decreasing trend with most of the heat flux occurring in the upper 500 m. The values of J_s reached $O(10^5)$ W/m^2 in the upper 200 m. J_s represents the heat flux in one of the ISWs, but clusters typically comprised large numbers of the ISWs with different amplitudes. To estimate the ISW contribution to the heat flux over the continental slope, we estimate the average heat flux (J_s^m) of the ISWs that were encountered during the observation. Profile of J_s^m is shown in Fig. 4a. J_s^m shows a decreasing trend with depth and most of the heat flux

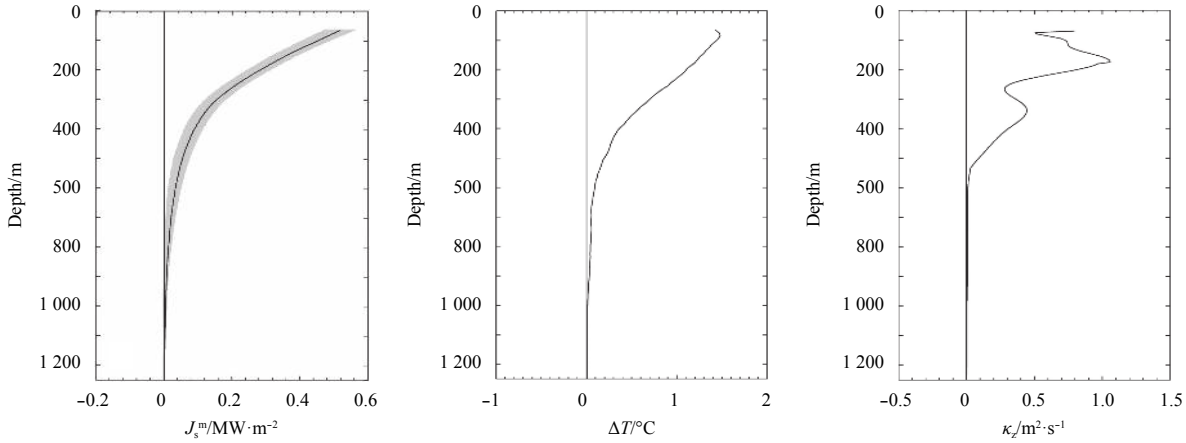

Fig. 4. Heat fluxes and vertical eddy diffusivity of the ISW. a. Averaged heat fluxes of the ISWs. The gray shading indicates the 95% bootstrapped confidence interval, b. ΔT as a function of depth, and c. κ_z as a function of depth calculated from the diffusion equation.

occurred in the upper 500 m. The divergence of heat flux in the ISWs is expressed through the one-dimensional balance $\Delta T = -\Delta t\,(\rho c_p)^{-1}\,(\mathrm{d}J_s^{\mathrm{m}}/\mathrm{d}z)$. Profile of ΔT is shown in Fig. 4b. Large averaged heat flux could change the temperature in the upper 500 m by 0.2 to 1.5°C with a mean value of 0.8°C. This implies that the ISWs are a significant contributor to the redistribution of heat over the continental slope.

The total heat transports of the ISWs were estimated as $E_Q = \int_{z_b}^{z_t} Q\mathrm{d}z$, where z_t and z_b represent the ocean surface and bottom, respectively. Q in each good temperature measurement depth bin was assumed to be constant with height over that depth bin. Here, we calculate E_Q by integrating Q between 65 and 1 250 m because there were few data in the upper 65 m, thus E_Q represents the total heat transport that was needed to achieve the temperature variations below 65 m. A summary of E_Q in the observed ISWs is given in Table 1. E_Q ranges from 0.56 to 2.83 GJ/m^2 with a mean of 1.63 GJ/m^2. E_Q shows large variation, similar to $\delta_{\max}$. To explore the relationship between E_Q and $\delta_{\max}$, a scatter plot between E_Q and $\delta_{\max}$ is shown in Fig. 5. E_Q displays a generally increasing trend with $\delta_{\max}$. An empirical linear fit between E_Q and $\delta_{\max}$ was obtained, E_Q=$\alpha\delta_{\max}$+β, where α=10.3 MJ/m^3 and β=0.88 GJ/m^2, are the fitting parameters.

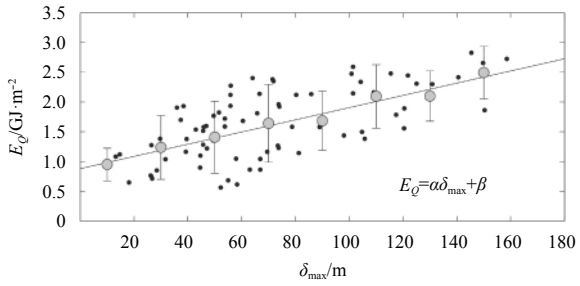

Fig. 5. Scatter plot and model fit between E_Q and $\delta_{\max}$. The small dots represent raw data and the large dots represent averages over a constant grid interval of 20 m. The straight line is a linear regression for bin-averaged samples. The vertical error bars correspond to 90% confidence limits of the bin-averaged E_Q.

To assess the efficacy of the model of E_Q=$\alpha\delta_{\max}$+β in predicting E_Q, we tested the linear regressions with t-test (Rice, 2006). The two-tailed test P-value estimated from the raw data and fitted values is 0.834. This value is greater than 0.05, which suggests that the null hypothesis cannot be rejected. The coefficients of determination (R^2) were also calculated to quantify how well the model can predict E_Q. R^2 is the ratio of the difference between the variance of the observed values and the variance of the residuals from the fit to the variance of the observed values (Rice, 2006). It can be interpreted as the proportion of the variability of the observed values that can be explained by the fitted values. The coefficient of determination between the bin-averaged data and the fitted values is 0.974, and the coefficient of determination between the raw data and the fitted values is 0.435.

4 Discussion

In the above analysis, we show that the ISWs can cause large temperature variation in the upper ocean after they pass the mooring. The temperature variation induced by the ISWs can be described by the following time-dependent conservation equation (Pope, 2000):

$$\partial T/\partial t = \nabla\cdot(\kappa\nabla T) - \nabla\cdot(\vec{v}T)\,, \tag{2}$$

where κ is the eddy diffusivity; $\vec{v}$ is the velocity field; ∇ is the gradient operator; and $\nabla\cdot$ is the divergence operator. The temperature variation comprises diffusive and advective components. The first contribution, $\nabla\cdot(\kappa\nabla T)$, describes the diffusion. The second contribution, $-\nabla\cdot(\vec{v}T)$, describes the advection, which is a transport mechanism of a conserved property by a fluid due to the fluid's bulk motion. Considering that diffusion is mainly dominant in the vertical direction and assuming that the velocity field describes an incompressible flow, then Eq. (2) can be simplified to

$$\frac{\partial T}{\partial t} = \frac{\partial}{\partial z}\left(\frac{\kappa_z \partial T}{\partial z}\right) - \left(U\frac{\partial T}{\partial x} + V\frac{\partial T}{\partial y} + W\frac{\partial T}{\partial z}\right), \tag{3}$$

where κ_z is the vertical eddy diffusivity; U, V and W are the zonal velocity, the meridional velocity, and the vertical velocity, respectively. Equation (3) implies that both advection and diffusion contribute to the temperature variation. Assuming that the advection term is 0 and the temperature variation just results from the diffusion, then Eq. (3) becomes the diffusion equation:

$$\frac{\partial T}{\partial t} = \frac{\partial}{\partial z}\left(\frac{\kappa_z \partial T}{\partial z}\right). \tag{4}$$

The contribution of the ISW-induced diffusion to the temperature variation has been reported by previous researchers (i.e., Inall et al., 2000; Moum et al., 2003). In these observations, the contribution of advection to the temperature variation appears to be less important compared with the diffusion. Their observations show that the temperature variation can be achieved by solving the diffusion equation with the observed eddy diffusivity and temperature gradients, or the eddy diffusivity can be estimated by solving the diffusion equation with the temperature variation. Taking the ISW that is shown in Fig. 3 as an example, we assume that the temperature variation only resulted from diffusion and solve the diffusion equation numerically with the temperature profile T_b following Inall et al. (2000). The diffusion time is set to 50 min, which corresponds to the time that was needed for the ISW to pass the mooring. The estimated κ_z profile is shown in Fig. 4c. The result indicates that κ_z in the upper 500 m needs to be larger than 10^{-1} m^2/s to achieve the temperature variation. However, the observations of Lien et al. (2012) indicate that the vertical eddy diffusivity of $O(10^{-1})$ m^2/s mainly occurred at the trapped core (in the upper 150 m) of a shoaling ISW. Our mooring was located over the continental slope. The ISWs arrived at the mooring as a nearly steady-state solitary depression wave. Vertical eddy diffusivity would not be larger than 10^{-1} m^2/s throughout the upper 500 m. Evidence can also be found in the depth-time map of shear $S = (\partial U/\partial z)^2 + (\partial V/\partial z)^2$ (Fig. 6a). Strong shear was mainly concentrated in the upper 150 m, whereas the shear below was weak and comparable to background values. These observations suggest that κ_z below 150 m should be smaller than 10^{-1} m^2/s. However, the profile of κ_z that was calculated from the diffusion equation shows κ_z of $O(10^{-1})$ m^2/s below 150 m (Fig. 4c). This difference suggests that in addition to diffusion, the advection also contributed to the observed temperature variation.

Evidence for the contribution of the advection to the temperature variation can be found in the velocity vector field of the ISW (Fig. 6b). We transformed the temporal variation in the ISW ob-

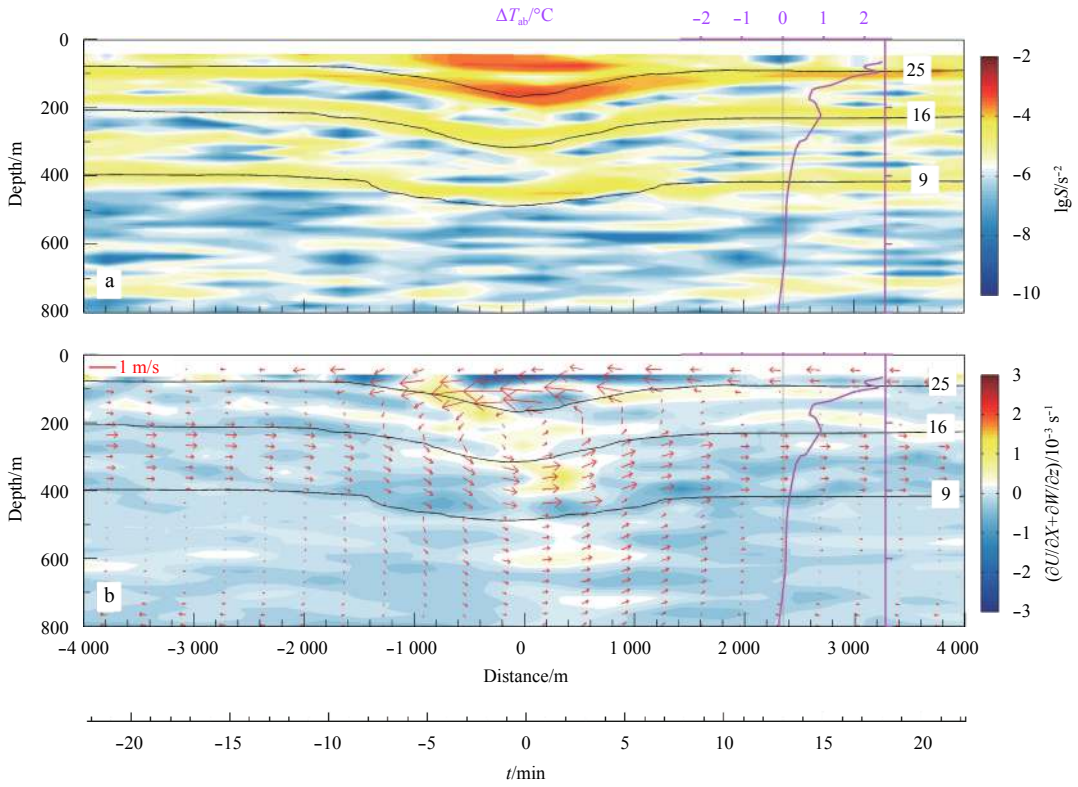

Fig. 6. Shear and velocity during the ISW. a. Map of the vertical shear $S = (\partial U/\partial z)^2 + (\partial V/\partial z)^2$, and b. map of the velocity divergences ($\partial U/\partial x + \partial W/\partial z$) and velocity vector fields (zonal and vertical velocities) of the ISW encountered on 251.15 d. The black lines in (a) and (b) indicate the 9, 16 and 25°C isotherms. The insets represent the temperature variation ΔT_{ab} (pink curves).

servations into the wave's spatial structure using a phase speed of 3.0 m/s. The velocity divergences $\nabla \cdot \vec{v}$ are also shown in Fig. 6b. The velocity divergences were estimated as $\partial U/\partial x + \partial W/\partial z$ because the ISW propagated principally westward and only $\partial U/\partial t$ can be converted into $\partial U/\partial x$ using the phase speed. This does not substantially impact our discussion because most of the horizontal velocities were contained in the zonal velocity during the passage of the ISW. It is apparent in Fig. 6b that the velocity divergences were approximately 0 for most of the depths during the observation period. The velocity divergences at some depths slightly deviated from 0, such as the velocity divergences in the upper 100 m, might be due to the absence of $\partial V/\partial y$. These observations indicated that $\nabla \cdot \vec{v}$=0 and the velocity field did not violate the conservation of mass.

The velocity field featured a "subsurface layer" (between the isotherms of 9 and 16°C) with relatively strong eastward velocity (Fig. 6b). Warm water was advected downward by the vertical velocity between –10 and 0 min (on the time axis), during which the warm water was also advected horizontally by the large eastward velocity in the subsurface layer. The vertical velocity changed direction at t=0 min and advected the warm water upward again between 0 and 10 min. However, the warm water could not be lifted up to its original depth by the upward vertical velocity. It was advected horizontally by the large eastward velocity before the vertical velocity lifted it because the upward vertical velocity was small and of short duration compared with the eastward velocity. The warm water that was advected horizontally by the eastward velocity led to a small peak value of ΔT_{ab} near the top of the subsurface layer. ΔT_{ab} below the subsurface layer was small because no large eastward velocity advected water horizontally and the water was again lifted by the upward vertical velocity. The velocity field slowly reverted to its original state between 10 and 25 min. Evidence of the contribution of the ISW-induced advection to the temperature variation was also observed in other ISWs (not shown).

To further explore the contribution of advection to the temperature variation, we quantified the changes in the vertical temperature gradient $\partial T/\partial z$ due to the passage of the ISW, which is

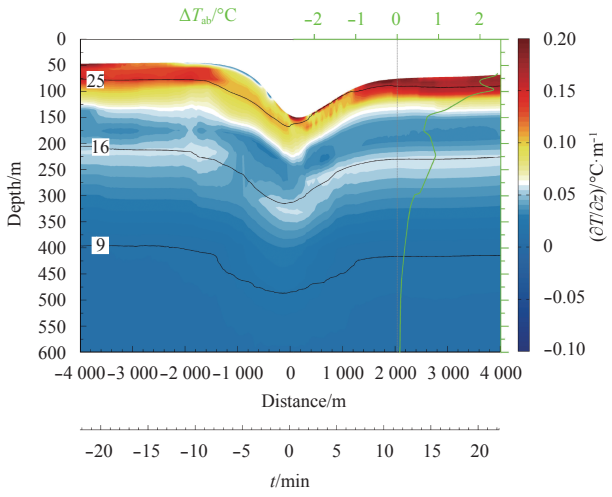

Fig. 7. Map of the vertical temperature gradient ($\partial T/\partial z$). The black lines indicate the 9, 16 and 25°C isotherms. The inset represents the temperature variation ΔT_{ab}.

shown in Fig. 7. $\partial T/\partial z$ in the upper 100 m was increased by approximately 0.05 after the passage (t>10 min) of the ISW, which might result from turbulent mixing since diffusion would redistribute the temperature field without moving the water. $\partial T/\partial z$ was also depressed downward after the passage of the ISW. As shown in Fig. 7 that the bottom of the large $\partial T/\partial z$ (>0.1°C/m) changed from a depth of approximately 100 m to a depth of approximately 110 m. This redistribution of $\partial T/\partial z$ mainly resulted from the advection. Both diffusion and advection contributed to the temperature variation in the upper 100 m. A different phenomenon occurred below 100 m. $\partial T/\partial z$ below 100 m suffered from the redistribution that was induced by the advection but not the diffusion (i.e., values of $\partial T/\partial z$ remained nearly unchanged), which is especially evident near the depth of the 16°C isotherm. $\partial T/\partial z$ near the depth of the 16°C isotherm was approximately 0.05°C/m and was depressed downward by approximately 20 m. This depression would increase the temperature by approximately 1°C to the observed ΔT_{ab} of 0.922°C. This suggests that the temperature variation below 100 m mainly resulted from the advection. Both vertical and horizontal velocities contributed to the redistribution of $\partial T/\partial z$. The warm water was first advected downward by the downward vertical velocity and was then lifted by the upward vertical velocity, during which the warm water was also advected by the horizontal velocity. The horizontal velocity trapped the warm water from being lifted, which led to the temperature variation. Similarly, the advection of the background horizontal temperature gradient ($\partial T_b/\partial x$) might also contribute to the temperature variation since large horizontal velocity occurred during the passage of the ISW. Here we roughly estimated $\partial T_b/\partial x$ with temperature data from Moorings A and B. $\partial T_b/\partial x$ is given by $\left(\overline{T_A}-\overline{T_B}\right)/\Delta d$, where $\overline{T_A}$ and $\overline{T_B}$ are the average temperatures at Moorings A and B, respectively; and Δd=22.13 km, is the horizontal separation between Moorings A and B. Taking a depth of 215 m as an example, we estimated $\partial T_b/\partial x$. The result indicated that $\partial T_b/\partial x$ at depth of 215 m was 1.38×10^{-6}°C/m. Thus an average horizontal velocity of 0.5 m/s that lasted for 180 min yields a temperature variation of 0.008°C, which is small compared with the observed value of 0.922°C. This suggests that the contribution of horizontal advection of $\partial T_b/\partial x$ to the temperature variation was small at depth of 215 m. Contribution of horizontal advection of $\partial T_b/\partial x$ to the temperature variation was also small at other depths (not shown).

Our estimates of J_s were calculated based on the temperature variation that was induced by the ISWs; thus, J_s comprised the contributions of the advection and the diffusion. They were larger than those observed over the continental shelf (Moum et al., 2003; Inall et al., 2000; Shroyer et al., 2010). Inall et al. (2000) estimated the average heat flux across the thermocline to be 80 W/m^2 over the Malin shelf; Moum et al. (2003) reported an instantaneous heat flux of O (10^3) W/m^2 over the continental shelf of Oregon; Shroyer et al. (2010) estimated the instantaneous heat flux in the ISWs to be 790 W/m^2 over New Jersey shelf. The larger heat flux in our observation can be attributed to a combination of factors. The ISW-induced advection is expected to be one of the factors. In previous observations over the continental shelf, the heat flux was primarily attributed to the ISW-induced diffusion. However, the ISW-induced advection also contributed to the heat flux in our observation. This difference might result from the properties of the ISWs. Previous observations were conducted over the continental shelf where the ISWs had shoaled. Small wavelength shear instabilities occurred in the ISWs, which caused the contribution of diffusion to the vertical heat transport to be more prominent than that of the advection. Our mooring was located over the continental slope. The ISWs were weakly non-linear and stable. Large velocities induced by the ISWs could advect the warm water downward, thus making an important contribution to the vertical heat transport. Unfortunately, we have no observed κ_z during the passage of the ISW to quantify how much of the heat flux was contributed by the ISW-induced advection and the ISW-induced diffusion, respectively. Additional data (i.e., microstructure data) are needed to solve this problem in the future.

5 Conclusions

Moored data obtained between 1 August and 27 September 2014 were used to explore the characteristic of the ISWs and estimate the vertical heat transport of the ISWs over the continental slope in the northern SCS. The clusters of the ISW packets were phase-locked to the fortnightly cycle of the semidiurnal tide. The ISWs appeared during large semidiurnal tides and there is a period of 5–6 d (during small semidiurnal tides) when no ISWs were observed. Our observation indicates that the ISWs can effectively modify the local temperature field in which the temperature increased as the ISWs passed the mooring. The increase in the temperature that was induced by the ISWs decreased with increasing depth and most of the temperature variation occurred in the upper 500 m. The heat flux that was estimated based on the temperature variation reached 0.01–0.1 MW/m^2 in the upper 500 m, which is one to three orders of magnitude larger than those observed over the continental shelf (Moum et al., 2003; Inall et al., 2000; Shroyer et al., 2010). The average heat flux in the ISWs would change the temperature in the upper 500 m by 0.2 to 1.5°C with a mean of 0.8°C, indicating that the ISWs are a significant contributor to the redistribution of heat in the upper ocean over the continental slope. Our observation suggests that both the ISW-induced diffusion and ISW-induced advection contributed to the heat flux. The diffusion and advection contributed to the temperature variation in the upper 100 m, and the advection made the domination contribution to the temperature variation below 100 m. The warm water was first advected downward by the downward vertical velocity and then lifted by the upward vertical velocity, during which the warm water was also advected by the horizontal velocity. The horizontal velocity trapped the warm water from being lifted to its original depth, which significantly improved the efficiency of the vertical heat transport. The estimated total heat transport, E_Q, ranged from 0.56 to 2.83 GJ/m^2 with a mean value of 1.63 GJ/m^2. E_Q was determined to be proportional to the maximum vertical displacement, such that $E_Q=\alpha\delta_{max}+\beta$. This model fitting provides a simple method for determining the vertical heat transport of the ISWs propagating over the continental slope in the northern SCS where only the vertical displacement (or velocity) is known. However, whether the model can be applied to other regions, such as the continental shelf, remains unknown. More observations are needed to robustly verify this model in the future.

Acknowledgements

We thank all the crew of the survey ship from the South China Sea Institute of Oceanology, Chinese Academy of Sciences.

References

Alford M H, Lien R C, Simmons H, et al. 2010. Speed and evolution of nonlinear internal waves transiting the South China Sea. Journal of Physical Oceanography, 40(6): 1338–1355, doi: 10.1175/2010JPO4388.1

Alford M H, MacKinnon J A, Nash J D, et al. 2011. Energy flux and dissipation in Luzon Strait: two tales of two ridges. Journal of Physical Oceanography, 41(11): 2211–2222, doi: 10.1175/JPO-D-11-073.1

Bai Xiaolin, Liu Zhiyu, Li Xiaofeng, et al. 2014. Generation sites of internal solitary waves in the southern Taiwan Strait revealed by MODIS true-colour image observations. International Journal of Remote Sensing, 35(11–12): 4086–4098, doi: 10.1080/01431161.2014.916453

Chen Zhiwu, Xie Jieshuo, Wang Dongxiao, et al. 2014. Density stratification influences on generation of different modes internal solitary waves. Journal of Geophysical Research, 119(10): 7029–7046

Choi W, Camassa R. 1999. Fully nonlinear internal waves in a two-fluid system. Journal of Fluid Mechanics, 396: 1–36, doi: 10.1017/S0022112099005820

Egbert G D, Erofeeva S Y. 2002. Efficient inverse modeling of barotropic ocean tides. Journal of Atmospheric and Oceanic Technology, 19(2): 183–204, doi: 10.1175/1520-0426(2002)019<0183:EIMOBO>2.0.CO;2

Guo C, Chen X. 2014. A review of internal solitary wave dynamics in the northern South China Sea. Progress in Oceanography, 121: 7–23, doi: 10.1016/j.pocean.2013.04.002

Hsu M K, Liu A K, Liu Cheng. 2000. A study of internal waves in the China seas and Yellow Sea using SAR. Continental Shelf Research, 20(4–5): 389–410, doi: 10.1016/S0278-4343(99)00078-3

Inall M E, Rippeth T P, Sherwin T J. 2000. Impact of nonlinear waves on the dissipation of internal tidal energy at a shelf break. Journal of Geophysical Research, 105(C4): 8687–8705, doi: 10.1029/1999JC900299

Inall M E, Shapiro G I, Sherwin T J. 2001. Mass transport by non-linear internal waves on the Malin shelf. Continental Shelf Research, 21(13–14): 1449–1472, doi: 10.1016/S0278-4343(01)00020-6

Klymak J M, Pinkel R, Liu C T, et al. 2006. Prototypical solitons in the South China Sea. Geophysical Research Letters, 33(11): L11607, doi: 10.1029/2006GL025932

Li Qiang, Farmer D M. 2011. The generation and evolution of nonlinear internal waves in the deep basin of the South China Sea. Journal of Physical Oceanography, 41(7): 1345–1363, doi: 10.1175/2011JPO4587.1

Lien R C, D'Asaro E A, Henyey F, et al. 2012. Trapped core formation within a shoaling nonlinear internal wave. Journal of Physical Oceanography, 42(4): 511–525, doi: 10.1175/2011JPO4578.1

Lien R C, Henyey F, Ma B, et al. 2014. Large-amplitude internal solitary waves observed in the northern South China Sea: properties and energetics. Journal of Physical Oceanography, 44(4): 1095–1115, doi: 10.1175/JPO-D-13-088.1

Lien R C, Tang T Y, Chang M H, et al. 2005. Energy of nonlinear internal waves in the South China Sea. Geophysical Research Letters, 32(5): L05615

Liu A K, Hsu M K. 2004. Internal wave study in the South China Sea using synthetic aperture radar (SAR). International Journal of Remote Sensing, 25(7–8): 1261–1264, doi: 10.1080/01431160310001592148

Liu A K, Ramp S R, Zhao Yunhe, et al. 2004. A case study of internal solitary wave propagation during ASIAEX 2001. IEEE Journal of Oceanic Engineering, 29(4): 1144–1156, doi: 10.1109/JOE.2004.841392

Moum J N, Farmer D M, Smyth W D, et al. 2003. Structure and generation of turbulence at interfaces strained by internal solitary waves propagating shoreward over the continental shelf. Journal of Physical Oceanography, 33(10): 2093–2112, doi: 10.1175/1520-0485(2003)033<2093:SAGOTA>2.0.CO;2

Orr M H, Mignerey P C. 2003. Nonlinear internal waves in the South China Sea: observation of the conversion of depression internal waves to elevation internal waves. Journal of Geophysical Research, 108(C3): 3064, doi: 10.1029/2001JC001163

Pope S B. 2000. Turbulent Flows. Cambridge: Cambridge University Press, 91–95

Ramp S R, Tang T Y, Duda T F, et al. 2004. Internal solitons in the northeastern South China Sea: Part I. Sources and deep water propagation. IEEE Journal of Oceanic Engineering, 29(4): 1157–1181

Ramp S R, Yang Y J, Bahr F L. 2010. Characterizing the nonlinear internal wave climate in the northeastern South China Sea. Nonlinear Processes in Geophysics, 17(5): 481–498, doi: 10.5194/npg-17-481-2010

Rice J A. 2006. Mathematical Statistics and Data Analysis. Australia: Nelson Education, 421–425

Shroyer E L, Moum J N, Nash J D. 2010. Vertical heat flux and lateral mass transport in nonlinear internal waves. Geophysical Research Letters, 37(8): L08601

Small J. 2001a. A nonlinear model of the shoaling and refraction of interfacial solitary waves in the ocean: Part I. Development of the model and investigations of the shoaling effect. Journal of Physical Oceanography, 31(11): 3163–3183

Small J. 2001b. A nonlinear model of the shoaling and refraction of interfacial solitary waves in the ocean: Part II. Oblique refraction across a continental slope and propagation over a seamount. Journal of Physical Oceanography, 31(11): 3184–3199

Xu Zhenhua, Liu Kun, Yin Baoshu, et al. 2016. Long-range propagation and associated variability of internal tides in the South China Sea. Journal of Geophysical Research, 121(11): 8268–8286

Xu Zhenhua, Yin Baoshu, Hou Yijun, et al. 2010. A study of internal solitary waves observed on the continental shelf in the northwestern South China Sea. Acta Oceanologica Sinica, 29(3): 18–25, doi: 10.1007/s13131-010-0033-z